Direct blending-drying method of graphitic carbon nitride (g-C$_3$N$_4$) with copper chloride solution for enhancement of photocatalytic decolorization of methylene blue

Ni Bai, Yongchao Qi, Xujian Miu, Jiahui Yin, Dandan Guo, Jinxi Wang, Aimin Wang[*]

Shaanxi Key Laboratory of Low Metamorphic Coal Clean Utilization, School Chemistry and Chemical Engineering, Yulin University, Yulin 71900 China

[*]Corresponding author, e-mail: aimin_wang@yulinu.edu.cn

ABSTRACT: A simple g-C$_3$N$_4$ and CuCl$_2$ composite catalyst (CN@CuCl$_2$) was prepared via direct blending-drying method and compared with ternary heterojunction series catalysts (CN/CuO/Cu$_2$O-x) and g-C$_3$N$_4$ disposed by copper chloride solution (CN/CuCl$_2$). The specific surface area and micropore surface area of g-C$_3$N$_4$ were increased after recombination with copper chloride, and the absorption range and ability of visible light were greatly enhanced, which showed the best photocatalytic activity. The degradation rate constant of high concentration methylene blue was about 2.6 times that of g-C$_3$N$_4$, and the degradation rate reached 59% after 180 min of illumination. This enhanced photocatalytic activity is mainly attributed to the ionic Z-scheme photocatalytic system, which relies on the charge transport of the electron mediator CuCl$_2$ (Cu^{2+}/Cu^{1+}) in the redox reaction to promote the photoexcited e$^-$ and h$^+$ separation and migration between g-C$_3$N$_4$ and Cu$_2$O.

KEYWORDS: graphite phase carbon nitride, copper chloride, MB, visible light, photocatalysis

INTRODUCTION

At present, with the rapid development of printing and dyeing industry, the widespread use of dyes brings about a large number of dye wastewater, which cause great harm to environment and human health. Photocatalysis is considered an ideal method for removing pollutants from wastewater and environmental remediation. However, the low solar energy utilization and light quantum conversion efficiency in visible region restrict the development of this technology [1–3].

The g-C$_3$N$_4$, as a typical polymeric layered semiconductor with stable heptazine ring structure has been investigated because of narrow band gap and wide absorption threshold, which enables it to absorb visible light energy in a certain wavelength range [4–7], is extensively studied in the field of photocatalytic hydrogen production [8,9], photocatalytic CO$_2$ reduction [10,11], and photocatalytic pollutant degradation [12,13]. However, pure g-C$_3$N$_4$ has the problems of small specific surface area, low quantum efficiency, and fast recombination of photo-generated carriers. So, many researchers often regulate the electronic structure through molecular level modification according to its flexible polymer structure. Various methods were developed to regulate electronic structure of g-C$_3$N$_4$, which included morphology control [14], metal-nonmetal doping [15,16], and forming heterojunction with other semiconductors [17,18]. Doping of metal elements such as Cu into the framework of g-C$_3$N$_4$ has been proven to increase visible light absorption and degradation rate of dye wastewater [19]. In spite of such advantages, the photocat-

alytic activity of Cu doped g-C$_3$N$_4$ is inhibited because of its high recombination rate of photo-generated e$^-$ and h$^+$. Hence, heterojunction forming between g-C$_3$N$_4$ and Cu$_2$O has been investigated to solve the problem by generating carrier separation and migration at the heterostructure interface [20–22]. It was found that the photocatalytic activity was significantly improved, but the stability needed to be improved.

Among all heterojunction catalytic systems, the direct Z-scheme photocatalytic system can not only promote separation of e$^-$ and h$^+$, but also preserve redox ability of its components. The direct Z-scheme heterojunction materials can be divided into ionic Z-scheme and solid Z-scheme heterojunction materials. Ionic Z-scheme photocatalytic material is a Z-scheme photocatalytic system which is studied earlier, and its reaction depends on the redox electron mediator. The solid Z-scheme photocatalytic material contains non-conductive and conductive media, which is different from that of the ionic photocatalytic system on photocatalytic mechanism of the photocatalytic system. Because of no redox electron mediator, electrons are directly transmitted through the interface, which shortens the transmission distance and improves the photocatalytic efficiency. For this purpose, g-C$_3$N$_4$ heterojunctions have been explored as possible as solid Z-scheme photocatalyts such as Ag/AgVO$_3$/carbon-rich g-C$_3$N$_4$ [23], AgBr/VO/P-g-C$_3$N$_4$ [24], g-C$_3$N$_4$/AgBr/Ag$_3$PO$_4$ [25], and g-C$_3$N$_4$/TiO$_2$/CdS [26], which exhibits higher photocatalytic degradation efficiency and stability [27–31].

Herein, g-C$_3$N$_4$ and CuCl$_2$ composite catalyst was prepared by a simple blending-drying method and

compared with ternary heterojunction series catalysts of g-C₃N₄/CuO/Cu₂O-x and g-C₃N₄ disposed by copper chloride solution of g-C₃N₄/CuCl₂. The structure, morphology, and optical properties of the catalysts were characterized by a series of analytical methods. The photocatalytic performances of the catalysts were evaluated by the efficiency of MB dye solution under visible light. Then, the possible reaction mechanisms of improving photocatalytic performance of g-C₃N₄ and photocatalytic degradation of MB were proposed.

MATERIALS AND METHODS

Chemicals

Dicyandiamide was supplied by Tianjin Fuchen Chemical Reagent Factory, China. $CuCl_2 \cdot 2H_2O$ was purchased from Tianjin Hongyan Chemical Reagent Factory, China. Methylene blue was from Tianjin Binhai Kedi Chemical Reagent Co., Ltd., China. All reagents were of analytical grade and used without further purification.

Synthesis of graphitic carbon nitride (CN) and ternary heterojunction catalysts of g-C₃N₄/CuO/Cu₂O-x (CN/CuO/Cu₂O-x)

Four grams of dicyandiamide was dissolved in 30 ml of hot deionized water, and 20 ml of CuCl₂ solution (0.04, 0.06, 0.08, and 0.10 mol/l, respectively) was slowly added into the solution under stirring. The mixed solution was heated, concentrated, and dried at 60 °C. The resulting residue was ground and put in a covered semi-closed crucible before placing in a muffle furnace. The heating rate was 2 °C/min, and the temperature was kept at 550 °C for 2 h. After natural cooling, the product was ground, impregnated with boiling water, and dispersed by ultrasound. Then, it was filtered, washed with hot water for three times, dried at 105 °C, and ground to obtain g-C₃N₄/CuO/Cu₂O-x catalysts (abbreviated as CN/CuO/Cu₂O-x; x refers to the molar concentration of CuCl₂ solution in mol/l). If 20 ml of deionize water was used instead of 20 ml of CuCl₂ solution and the other steps were the same as above, g-C₃N₄ was obtained.

Preparation of g-C₃N₄ and CuCl₂ composite catalyst (CN@CuCl₂) and g-C₃N₄ disposed by CuCl₂ solution (CN/CuCl₂)

The prepared CN above was dispersed in 20 ml of 0.06 mol/l CuCl₂ solution. Then, it was boiled, concentrated, dried at 105 °C, and ground to obtain g-C₃N₄ and CuCl₂ composite catalyst. After CN@CuCl₂ was impregnated with boiling water and dispersed by ultrasound, it was filtered, washed with hot water for three times, dried and ground at 105 °C to obtain the g-C₃N₄ disposed by CuCl₂ solution, which was denoted as CN/CuCl₂.

Characterizations of the photocatalysts

The crystal phases of catalysts were characterized by X-ray diffractometer (XRD, Shimadzu XRD-7000, Japan) with Cu K_α (λ=0.15406 nm, 6°/min from 5° to 80°). The micromorphology of catalysts was observed by a field-emission scanning electron microscopy (SEM, Zeiss Sigma300, Germany) equipped with energy dispersive spectroscopy (EDS). The chemical composition and valence band position of catalysts were measured by X-ray photoelectron spectroscopy (XPS, Escalab 250 Xi, Thermo Fisher, USA), and C 1s (284.8 eV) was used as the calibration peak for charge correction. The optical characteristics were carried out by UV-Vis diffuse reflectance spectrum (UV-Vis DRS, Shimadzu UV-2450, Japan) with BaSO4 taken as a reference material. The infrared spectra were recorded using Fourier transform infrared spectra (FTIR, Bruker Tensor 27, USA) with wavenumber range of 4000–5000 cm⁻¹. The pore size distribution and specific surface area were analyzed by specific surface area and pore size analysis equipment (BET, Gold APP V-sorb 2800TP, China).

Photocatalytic activity measurements

The as-prepared photocatalysts were evaluated via degradation of MB under visible light irradiation. The 0.1 g of catalyst was distributed to 50 ml of MB (100 mg/l) solution. The suspension was stirred vigorously for 1 h at room temperature in the dark. Subsequently, the degradation reaction was conducted under the light from a 480 W xenon lamp. The reaction solution was drawn at regular intervals and filtered through a 0.45 μm microfiltration membrane. Finally, the diluted solution was used to determine the absorbance by UV-vis spectrometer at its characteristic peak of 664 nm.

RESULTS AND DISCUSSION

Characterizations of the photocatalysts

The XRD patterns of the as-prepared catalysts are shown in Fig. 1. As depicted in Fig. 1a, pure CN sample revealed 2 obvious characteristic peaks at 2θ=13.0° and 27.3°, corresponding to (100) and (002) crystal face of g-C₃N₄ [32], respectively, and weak impurity peaks appear at 2θ=44.1°, 64.5°, and 77.6° because of incomplete decomposition and carbonization of dicyandiamide. For CN/CuO/Cu₂O-x, the intensity of diffraction peaks for CN was not decreased, whereas the XRD peaks of copper oxide gradually appeared at 2θ=35.5°, 38.7°, 38.9°, and 48.6° with the increase copper chloride added. For CN@CuCl₂, directly adding of copper chloride solution remarkably weakened the diffraction intensity of CN, and the strong XRD peaks appeared at 2θ=16.2°, 22.0°, 28.9°, and 34.0°, which belong to copper chloride dihydrate ($CuCl_2 \cdot 2H_2O$). For CN/CuCl₂, the intensity of CN diffraction peak did not change after being disposed by copper chloride solution, and no obvious phase was observed. Fig. 1b
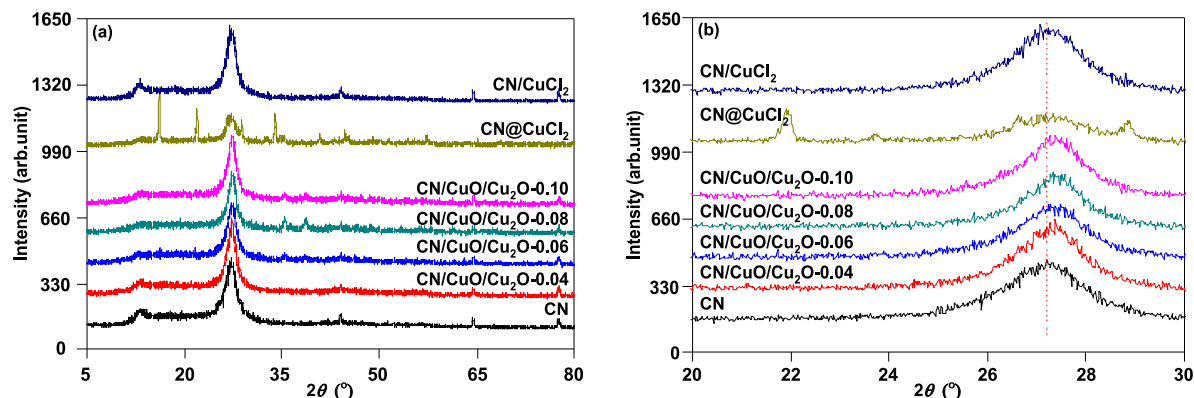
Fig. 1 XRD patterns of the as-prepared catalysts.

shows the enlarged view of Fig. 1a at $2\theta=20°\sim30°$. Among the 3 modification methods of CN, the diffraction peak of the (002) crystal face for CN/CuO/Cu$_2$O-x gradually moved to a high angle, which may be caused by the copper oxide generated by copper chloride decomposition entering the lattice of CN and changing the interlayer spacing of the layered structure.

As demonstrated in Fig. S1, all samples showed similar absorption peaks between 3148 and 3282 cm^{-1} corresponding to O—H stretching vibration peaks and N—H stretching vibration peaks. The peaks between 1244 and 1637 cm^{-1} that were 1244, 1317, 1407, 1459, 1571, and 1637 cm^{-1} are C—N and C=N stretching vibration peaks. The peak at 888 cm^{-1} is N—H deformation peak, and 806 cm^{-1} corresponds to the structural characteristic peak of CN heptazine. The existence of absorption peaks of 806 cm^{-1} and 1244~1637 cm^{-1} proves that all samples have a heptazine phase structure (3-s-triazine ring).

It was observed that CN had an irregular lamellar morphology, which is formed by the polycondensation of dicyandiamide (Fig. 2). The CN/CuO/Cu$_2$O-0.10 is composed of stacking blocks of different sizes. In addition, C, N, O, and Cu are reflected in EDS analysis and indicate that Cu is uniformly distributed in crystal structure of CN. The atomic ratio of C/N greatly exceeded 0.77 of CN, indicating that carbon-rich CN has been generated in CN/CuO/Cu$_2$O-0.10. The C, N, O, Cl, and Cu in CN@CuCl$_2$ were detected, which shows the presence of copper chloride. After removing copper chloride by washing with hot water, the CN/CuCl$_2$ was obtained, and the surface became loose and porous. The atomic ratio of C/N was basically the same as CN.

As demonstrated in Fig. S2 and Table 1, both catalysts presented Type IV isotherms with an average pore diameter of about 45 and 43 nm, respectively, indicating that both catalysts are mesoporous materials. The specific surface areas of CN and CN@CuCl$_2$ calculated by BET method were 4.51 m^3/g and 5.73 m^3/g respectively, which indicates that after the recombination of CN and copper chloride, the micropore surface area is greatly increased, resulting in a large increase in specific surface area.
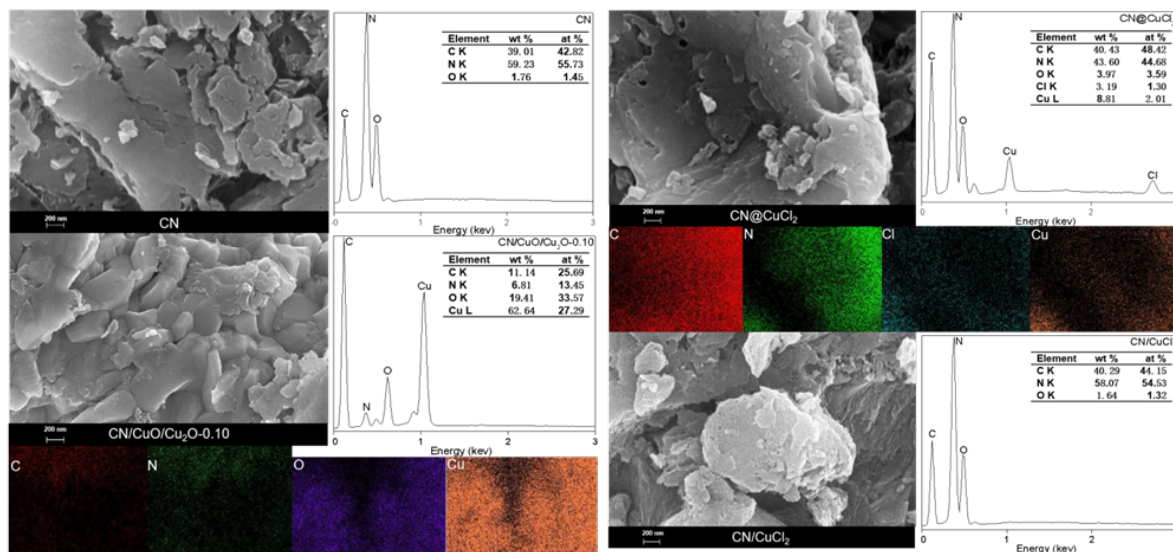
The optical properties of the as-prepared catalysts were investigated by UV-Vis DRS. As illustrated in Fig. 3a, pure CN showed a narrow absorption edge at about 440 nm, whereas the absorption edge moved slightly to visible region after being modified with copper chloride solution. Among them, the maximum absorption edge of CN@CuCl$_2$ was about 477 nm, indicating that the blending-drying of CN and copper chloride significantly broadens light absorption range. The E_g of catalysts can be calculated according to Kubelka-Munk equation [33].

$$\alpha h\nu = A(E_g - h\nu)^{n/2}$$

where α, h, ν, and E_g are absorbance, Planck's constant, photon frequency, and band gap energy, respectively [34]. The value of n depends on the type of semiconductor's transition characteristic (direct transition $n = 1$ or indirect transition $n = 4$).

As shown in Fig. 3b, the E_g of CN, CN/CuCl$_2$, CN/CuO/Cu$_2$O-0.04, CN/CuO/Cu$_2$O-0.10, CN/CuO/Cu$_2$O-0.06, CN/CuO/Cu$_2$O-0.08, and CN@CuCl$_2$ were 2.68, 2.68, 2.45, 2.43, 2.37, 2.34, and 2.31 eV, respectively, which were calculated from $(\alpha h\nu)^{1/2}$ via $h\nu$. Among all samples, CN@CuCl$_2$ showed wider and stronger absorption of visible light, which can produce more e$^-$-h$^+$ pairs and then improve photocatalytic performance.

As illustrated from XPS survey spectra in Fig. 4a, 3 main elements existing in CN were C, N, and O. The C and N are component of CN, while O element is derived from water molecules or oxygen adsorbed by the sample. In addition, the Cu and Cl element were obviously detected in CN/CuO/Cu$_2$O-0.10 and CN@CuCl$_2$, respectively, and a little Cu element also presented in CN/CuCl$_2$. In the C 1s spectrum of CN (Fig. 4b), the 2 strong peaks centered in 287.9 and 288.9 eV correspond to C atom (N=C—N) of sp^2 hybridization, while another weak peak at 284.8 eV belongs to the C atom in the graphite-like structure.

Fig. 2 SEM images of CN, CN/CuO/Cu$_2$O-0.10, CN@CuCl$_2$, and CN/CuCl$_2$ and EDS corresponding to CN/CuO/Cu$_2$O-0.10 and CN@CuCl$_2$.
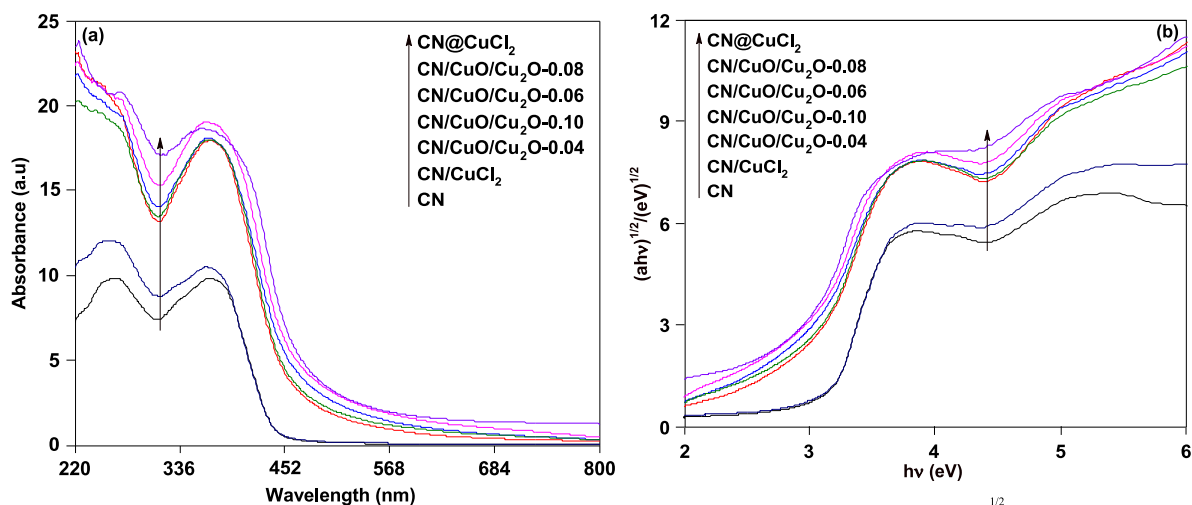
Table 1 Characteristics of CN and CN@CuCl$_2$

Sample	Specific surface area (m^2/g)			d_m	Pore volume
	S$_{BET}$[a]	S$_{ext}$[b]	S$_{mic}$[c]	(nm)	(cm^3/g)
CN	4.51	2.89	1.62	45.31	0.06
CN@CuCl$_2$	5.73	1.58	4.15	43.36	0.05

[a] S$_{BET}$ (BET surface area) determined by BET model; [b] S$_{ext}$, external surface area; and [c] S$_{mic}$, micropore surface area, and d_m calculated by BJH method from desorption branch.

The N 1s binding energies of CN in Fig. 4c were located at 398.4, 399.4, and 404.4 eV and belong to the N atom in C=N−C bond of sp^2 hybridization, N−(C)$_3$ bond of 3-s-triazine ring and NH$_2$, and NH bond of the terminal amino functional group, respectively. The C 1s and N 1s binding energy (BE) of CN changed from 0.2 to 2.6 eV after copper chloride solution treatment.

From Fig. 4d, the Cu 2p spectrum consisted of

Fig. 3 UV-Vis DRS spectra (a) and the diagrams of the $(\alpha h\nu)^{1/2}$ via $h\nu$ (b) over as-prepared catalysts.
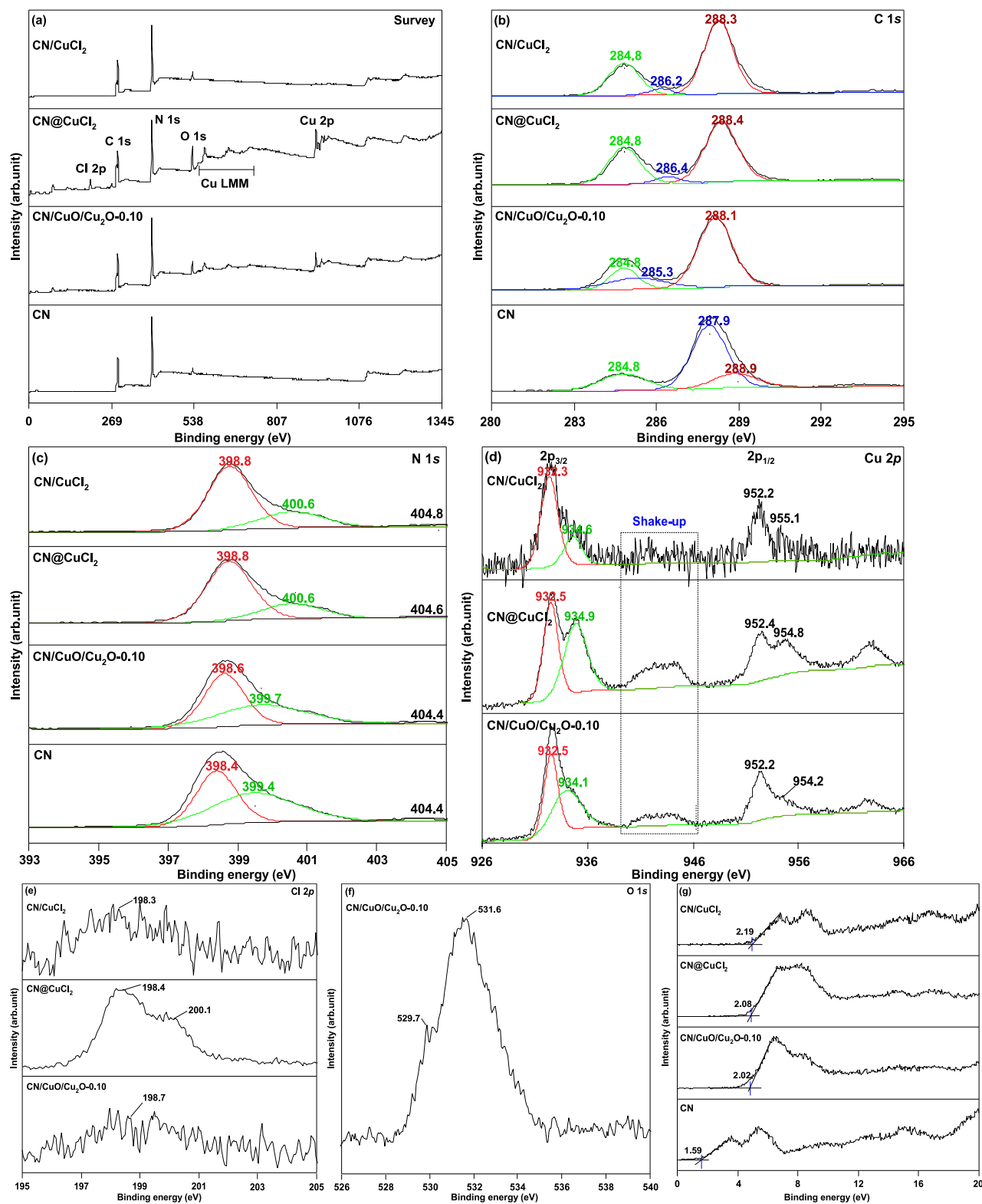
Fig. 4 XPS spectra of survey (a), C 1s (b), N 1s (c), Cu 2p (d), Cl 2p (e), O 1s (f), and VB (g) of the as-prepared catalysts.

the strongest Cu $2p_{3/2}$ peak (932.5∼934.9 eV) and the weaker Cu $2p_{1/2}$ peak (952.2∼954.8 eV), and the existence of shake-up peak indicated the presence of Cu^{2+} species [35]. There was a small shake-up peak in the $CN/CuCl_2$ spectrum, and Cu $2p_{3/2}$ peak could be fitted to 2 peaks belonging to Cu^{1+} at 932.3 eV and Cu^{2+} at 934.6 eV. The Cu^{1+}/Cu^{2+} valence ratio of $CN/CuCl_2$, $CN@CuCl_2$, and $CN/CuO/Cu_2O$-0.10 were 1.59, 0.93, and 1.72, respectively, indicating that part of Cu^{2+} is reduced to Cu^{1+} during CN modification by Cu^{2+}.

The Cl 2p spectrum of $CN@CuCl_2$ showed 2 main peaks, as compared in Fig. 4e. The strong peak located at a low BE of 198.4 eV is the ionic Cl atom (Cl^-), while the weak peak of 200.1 eV belongs to the covalent Cl atom (C−Cl) [36]. As shown from the O 1s spectrum for $CN/CuO/Cu_2O$-0.10 in Fig. 4f, the weak peak with BE at 529.7 eV is attributed to lattice O atoms, and the strong peak at 531.6 eV corresponds to O atoms in hydroxyl or moisture. The XPS analysis results of all catalysts are summarized in Table S1.

The valence band (VB) energy level position of CN was 1.59 eV, while the VB energy level of $CN/CuO/Cu_2O$-0.10, $CN@CuCl_2$ and $CN/CuCl_2$ moved to the direction of high binding energy, which were located at 2.02, 2.08, and 2.19 eV, respectively (Fig. 4g). Combined with analysis result of UV-Vis DRS, the conduction band (CB) energy levels of CN, $CN/CuO/Cu_2O$-0.10, $CN@CuCl_2$, and $CN/CuCl_2$ were calculated to be the −1.09, −0.41, −0.23, and −0.49 eV, respectively, as demonstrated in Fig. S3. The results showed that the method of copper chloride modification not only changes the energy band width of CN, but also adjusts its VB and CB energy levels.

The photocatalytic performance of the catalysts was evaluated by degradation of high concentration MB under visible light. As shown in Fig. 5, before the xenon lamp was turned on, the removal rate of MB by CN adsorption was about 12%, and the adsorption performance became stronger after copper chloride modification treatment. The photocatalytic performance of CN modified by copper chloride was better than CN when xenon lamp was turned on. The degradation rate of MB by $CN@CuCl_2$ reached 59% after 180 min of illumination. It is now generally accepted that the degradation kinetic curve follows the pseudo-first-order kinetic model: $-\ln(C/C_0) = kT$. Through fitting calculation, the rate constants k of CN, $CN/CuO/Cu_2O$-0.04, $CN/CuO/Cu_2O$-0.06, $CN/CuO/Cu_2O$-0.08, $CN/CuO/Cu_2O$-0.10, $CN/CuCl_2$, and $CN@CuCl_2$ were 0.0016, 0.0019, 0.0017, 0.0019, 0.0014, 0.0017, and 0.0041 min^{-1}, respectively. The $CN@CuCl_2$ showed the maximum rate constant, which is about 2.6 times that of CN. It is due to ionic Z-scheme photocatalytic system formed by composition of CN and copper chloride, which increases the specific surface area of the catalyst, reduces the energy band
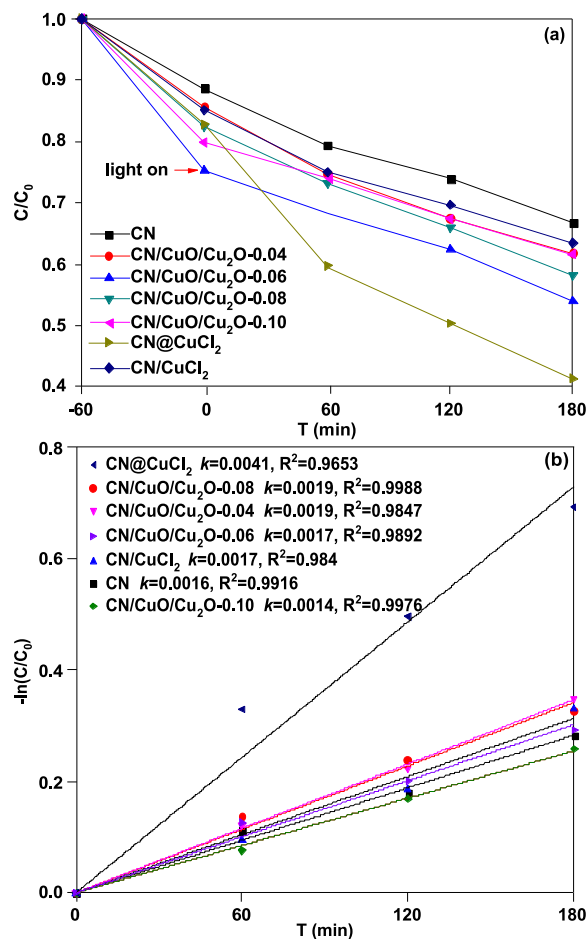

Fig. 5 Degradation curves (a) and kinetic fitting curves (b) of MB by catalysts under visible light.
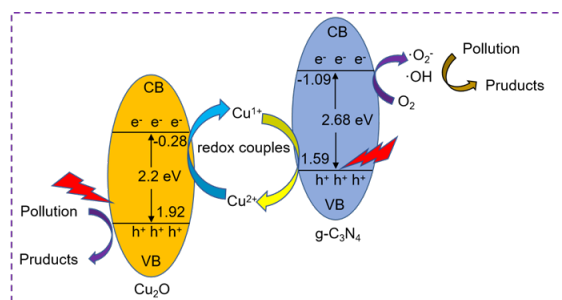

Fig. 6 Mechanism diagram of $CN@CuCl_2$ for MB degradation.

width, and separates e^- and h^+ effectively, thereby improving the quantum efficiency.

On basis of the above analysis, the possible electron transfer mechanisms of catalysts were analyzed. The ternary heterostructure series catalysts of $CN/CuO/Cu_2O$-x are mainly composed of g-C_3N_4, CuO, and Cu_2O, which can all be excited to generate e^-

and h$^+$ under visible irradiation. The e$^-$ will gather on CB of the more positive potential CuO semiconductor, and h$^+$ is enriched on VB of the more negative potential g-C$_3$N$_4$. Thus, e$^-$ and h$^+$ are effectively separated to improve quantum efficiency. The CN/CuCl$_2$ is the product of Cu^{2+} adsorption and reduction reaction of g-C$_3$N$_4$. A small amount of Cu$_2$O was detected on the surface with the less amount of CuO. Due to the small amount of loading, the photocatalytic activity of CN/CuCl$_2$ for g-C$_3$N$_4$ is not improved much. Therefore, we can confirm that CN@CuCl$_2$ mainly consists of g-C$_3$N$_4$ and CuCl$_2$ and a small amount of Cu$_2$O. The mechanism diagram of CN@CuCl$_2$ for MB degradation is shown in Fig. 6. The reduction potential of Cu^{2+}/Cu$^+$ is +0.135 V vs. NHE. The VB of Cu$_2$O is excited by light with the e$^-$ transition to CB; h$^+$ in VB can directly oxidize MB to CO$_2$, H$_2$O, etc., while e$^-$ in CB is caught by Cu^{2+} to generate Cu^{1+} and is consumed. The VB of g-C$_3$N$_4$ is excited by light with the e$^-$ transition to the CB captured with the adsorbed O$_2$ on the surface to form O$_2^-\cdot$ and then combined with H$^+$ to form HOO$\cdot$ until $\cdot$OH is formed. O$_2^-\cdot$ and $\cdot$OH can oxidize MB, and h$^+$ in VB reacts with Cu^{1+} to form Cu^{2+}. So, it should be an ionic Z-scheme photocatalytic system, and the reaction depends on the charge transfer of the redox reaction electron mediator CuCl$_2$ (Cu^{2+}/Cu^{1+}). It not only broadens the light response range and reduces photo-generated e$^-$ and h$^+$ recombination, but also maintains the oxidation ability of Cu$_2$O and reduction ability of g-C$_3$N$_4$.

CONCLUSION

The ternary heterojunction series catalysts of CN/CuO/Cu$_2$O-x were synthesized *in situ* with dicyandiamide and copper chloride by thermal polymerization method. The g-C$_3$N$_4$ and CuCl$_2$ solution were mixed and dried to obtain ionic Z-scheme photocatalyst of CN@CuCl$_2$ which is mainly composed of g-C$_3$N$_4$, Cu$_2$O, and CuCl$_2$. Continuous washing and drying with hot water for many times, CN/CuCl$_2$ could be obtained. After copper chloride doping modification, the surface morphology of g-C$_3$N$_4$ was changed, and the VB position of the catalysts was increased, and E_g was narrowed. At the same time, copper oxide produced by copper chloride decomposition at high temperature was doped into the lattice gap of g-C$_3$N$_4$, which has a significant impact on the photocatalytic activity of the catalyst. The formation of ionic Z-scheme photocatalyst of CN@CuCl$_2$ increased the specific surface area and micropore volume of g-C$_3$N$_4$. Compared with ternary heterojunction catalyst of CN/CuO/Cu$_2$O-0.10, it can not only ensure a wide visible light response range, but also maintain the corresponding oxidation and reduction capabilities of Cu$_2$O and g-C$_3$N$_4$. It shows the best photocatalytic performance, and the rate constants was about 2.6 times that of g-C$_3$N$_4$. The degradation rate of high concentration MB reached 59% under 180 min illumination.

REFERENCES

1. Wang Y, Wang XC, Antoniettie M (2012) Polymeric graphitic carbon nitride as a heterogeneous organocatalyst: From photochemistry to multipurpose catalysis to sustainable chemistry. *Angew Chem Int Edit* **51**, 68–89.
2. Zhang JL, Wu YM, Xing MY, Leghari SAK, Sajjad S (2010) Development of modified N doped TiO$_2$ photocatalyst with metals, nonmetals and metal oxides. *Energ Environ Sci* **3**, 715–726.
3. Chen XB, Shen SH, Guo LJ, Mao SS (2010) Semiconductor-based photocatalytic hydrogen generation. *Chem Rev* **110**, 6503–6570.
4. Lian K, Thorpe SJ, Kirk DW (1992) Electrochemical and surface characterization of electrocatalytically active amorphous Ni/Co alloys. *Electrochim Acta* **37**, 2029–2041.
5. Yan XD, Tian LH, Chen XB (2015) Crystalline/amorphous Ni/NiO core/shell nanosheets as highly active electrocatalysts for hydrogen evolution reaction. *J Power Sources* **300**, 336–343.
6. Bi LL, Xu DD, Zhang LJ, Lin YH, Xie TF (2015) Metal Ni-loaded g-C$_3$N$_4$ for enhanced photocatalytic H$_2$ evolution activity: the change in surface band bending. *Phys Chem Chem Phys* **17**, 29899–29905.
7. Lv YH, Liu YF, Zhu YY, Zhu YF (2014) Surface oxygen vacancy induced photocatalytic performance enhancement of a BiPO$_4$ nanorod. *J Mater Chem A* **2**, 1174–1182.
8. Wang XC, Maeda K, Thomas A, Takanabe K, Xin G, Carlssonc JM, Domen K, Antoniettie M (2009) A metal-free polymeric photocatalyst for hydrogen production from water under visible light. *Nat Mater* **8**, 76–80.
9. Kudo A, Miseki Y (2009) Heterogeneous photocatalyst materials for water splitting. *Chem Soc Rev* **38**, 253–278.
10. Niu P, Yang YQ, Yu JC, Liu G, Cheng HM (2014) Switching the selectivity of the photoreduction reaction of carbon dioxide by controlling the band structure of a g-C$_3$N$_4$ photocatalyst. *Chem Commun* **50**, 10837–10840.
11. Wang K, Li Q, Liu BS, Cheng B, Ho WK, Yu JG (2015) Sulfur-doped g-C$_3$N$_4$ with enhanced photocatalytic CO2-reduction performance. *Appl Catal B Environ* **176–177**, 44–52.
12. Sano T, Tsutsui S, Koike K, Hirakawa T, Teramoto Y, Negishi N, Takeuchi K (2013) Activation of graphitic carbon nitride (g-C$_3$N$_4$) by alkaline hydrothermal treatment for photocatalytic NO oxidation in gas phase. *J Mater Chem A* **1**, 6489–6496.
13. Yan SC, Li ZS, Zou ZG (2009) Photodegradation performance of g-C$_3$N$_4$ fabricated by directly heating melamine. *Langmuir* **25**, 10397–10401.

14. Han CC, Ge L, Chen CF, Li YJ, Xiao XL, Zhang YN, Guo LL (2014) Novel visible light induced Co_3O_4-g-C_3N_4 heterojunction photocatalysts for efficient degradation of methyl orange. *Appl Catal B Environ* **147**, 546–553.

15. Bai N, Yin JH, Huo XX, Ma YJ, Guo DD, Wang AM (2022) *In situ* synthesis of sodium doped g-C_3N_4 by high temperature copolymerization and photocatalytic performance. *ScienceAsia* **48**, 202–208.

16. Wu M, Zhang J, He BB, Wang HW, Wang R, Gong YS (2019) *In situ* construction of coral-like porous P-doped g-C_3N_4 tubes with hybrid 1D/2D architecture and high efficient photocatalytic hydrogen evolution. *Appl Catal B Environ* **241**, 159–166.

17. Sun LM, Qi Y, Jia CJ, Jin Z, Fan WL (2014) Enhanced visible-light photocatalytic activity of g-C_3N_4/Zn_2GeO_4 heterojunctions with effective interfaces based on band match. *Nanoscale* **6**, 2649–2659.

18. Zhou S, Liu Y, Li JM, Wang YJ, Jiang GY, Zhao Z, Wang DX, Duan AJ, et al (2014) Facile in situ synthesis of graphitic carbon nitride (g-C_3N_4)-N-TiO_2 heterojunction as an efficient photocatalyst for the selective photoreduction of CO_2 to CO. *Appl Catal B Environ* **158**, 20–29.

19. Li XW, Wang B, Yin WX, Di J, Xia JX, Zhu WS, Li HM (2020) Cu^{2+} modified g-C_3N_4 photocatalysts for visible light photocatalytic properties. *Acta Phys Chim Sin* **36**, 123–132.

20. Zhang SS, Yan J, Yang SY, Xu YH, Cai X, Li X, Zhang XC, Peng F, et al (2017) Electrodeposition of Cu_2O/g-C_3N_4 heterojunction film on an FTO substrate for enhancing visible light photoelectrochemical water splitting. *Chinese J Catal* **38**, 365–371.

21. Zuo SY, Xu HM, Liao W, Yuan XJ, Sun L, Li Q, Zan J, Li DY, et al (2018) Molten-salt synthesis of g-C_3N_4-Cu_2O heterojunctions with highly enhanced photocatalytic performance. *Colloid Surface A* **546**, 307–315.

22. Dai BL, Li YY, Xu JM, Sun C, Li SJ, Zhao W (2022) Photocatalytic oxidation of tetracycline, reduction of hexavalent chromium and hydrogen evolution by Cu_2O/g-C_3N_4 S-scheme photocatalyst: performance and mechanism insight. *Appl Surf Sci* **592**, 153309.

23. Liu ZX, Liu YD, Sun XB, Ji HD, Liu W, Cai ZQ (2022) Construction of Z-scheme Ag/$AgVO_3$/carbon-rich g-C_3N_4 heterojunction for enhanced photocatalytic degradation of sulfamethiadiazole: DFT calculation and mechanism study. *Chem Eng J* **433**, 133604.

24. Raizada P, Sudhaik A, Singh P, Hosseini-Bandegharaei A, Thakur P (2019) Converting type II AgBr/VO into ternary Z scheme photocatalyst via coupling with phosphorus doped g-C_3N_4 for enhanced photocatalytic activity. *Sep Purif Technol* **227**, 115692.

25. Shi WL, Liu C, Li MY, Lin X, Guo F, Shi JY (2020) Fabrication of ternary Ag_3PO_4/$Co_3(PO_4)_2$/g-C_3N_4 heterostructure with following Type II and Z-Scheme dual pathways for enhanced visible-light photocatalytic activ-ity. *J Hazard Mater* **389**, 121907.

26. Liu YY, Tian J, Wei LY, Wang Q, Wang C, Xing Z, Li X, Yang W, et al (2021) Modified g-C_3N_4/TiO_2/CdS ternary heterojunction nanocomposite as highly visible light active photocatalyst originated from CdS as the electron source of TiO_2 to accelerate Z-type heterojunction. *Sep Purif Technol* **257**, 117976.

27. Yang Q, Li RJ, Wei SQ, Yang R (2022) Schottky function-alized Z-scheme heterojunction photocatalyst Ti_2C_3/g-C_3N_4/BiOCl: Efficient photocatalytic H_2O_2 production via two-channel pathway. *Appl Surf Sci* **572**, 151525.

28. Yan S, Cai ZL, Wu D, Yu YL, Huang SL, Cao YA (2021) Z-scheme interface modification by MnV_2O_6 for V_2O_5/g-C_3N_4 heterostructure towards efficient visible photocat-alytic activity. *J Alloy Compd* **882**, 160751.

29. Li YZ, Wang XS, Wang XJ, Xia YS, Zhang AM, Shi JH, Gao LZ, Wei H, et al (2021) Z-scheme $BiVO_4$/g-C_3N_4 heterojunction: an efficient, stable and heterogeneous catalyst with highly enhanced photocatalytic activity towards Malachite Green assisted by H_2O_2 under visible light. *Colloid Surface A* **618**, 126445.

30. Hua SX, Qu D, An L, Jiang WS, Wen YJ, Wang XY, Sun ZC (2019) Highly efficient p-type Cu_3P/n-type g-C_3N_4 photocatalyst through Z-scheme charge transfer route. *Appl Catal B Environ* **240**, 253–261.

31. Wang YY, Huang HL, Zhang ZZ, Wang C, Yang YY, Li Q, Xu DS (2021) Lead-free perovskite $Cs_2AgBiBr_6$@g-C_3N_4 Z-scheme system for improving CH_4 production in photocatalytic CO_2 reduction. *Appl Catal B Environ* **282**, 119570.

32. Zhao XS, You YY, Huang SB, Wu YX, Ma YY, Zhang G, Zhang ZH (2020) Z-scheme photocatalytic produc-tion of hydrogen peroxide over $Bi_4O_5Br_2$/g-C_3N_4 het-erostructure under visible light. *Appl Catal B Environ* **278**, 119251.

33. Yang L, Bai X, Shi J, Du XY, Xu L, Jin PK (2019) Quasi-full-visible-light absorption by D35-TiO_2/g-C_3N_4 for synergistic persulfate activation towards efficient photodegradation of micropollutants. *Appl Catal B En-viron* **256**, 117759.

34. Zhao W, Guo Y, Faiz Y, Yuan WT, Sun C, Wang SM, Deng YH, Zhuang Y, et al (2015) Facile *in situ* synthesis of Ag/$AgVO_3$ one-dimensional hybrid nanoribbons with enhanced performance of plasmonic visible-light photo-catalysis. *Appl Catal B Environ* **163**, 288–297.

35. Espinós JP, Morales J, Barranco A, Caballero A, Holgado JP, González-Elipe AR (2002) Interface effects for Cu, CuO, and Cu_2O deposited on SiO_2 and ZrO_2. XPS deter-mination of the valence state of copper in Cu/SiO_2 and Cu/ZrO_2 catalysts. *J Phys Chem B* **106**, 6921–6929.

36. Yang W, Shan Y, Ding S, Han X, Liu YX, Pan JF (2019) Gas-phase elemental mercury removal using ammonium chloride impregnated sargassum chars. *Environ Technol* **40**, 1923–1936.
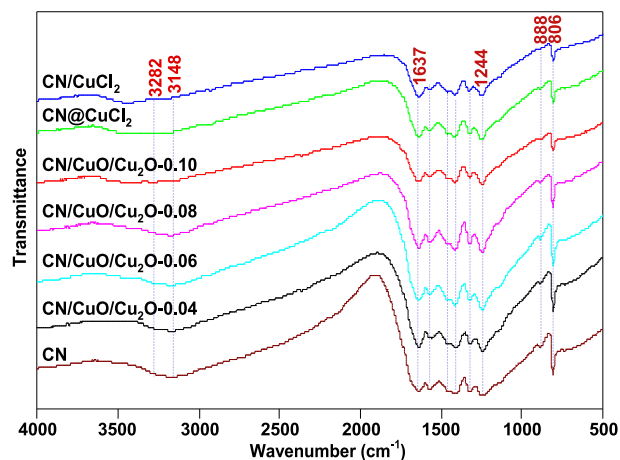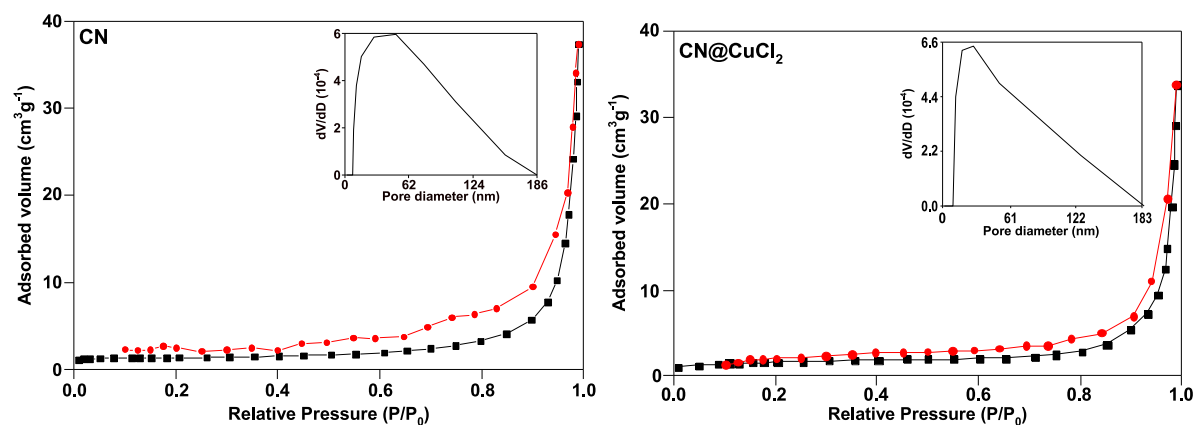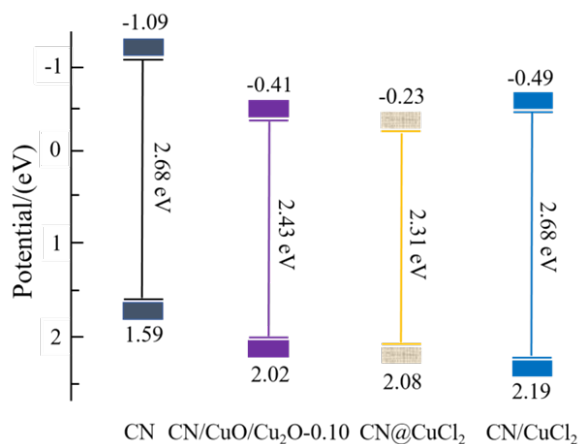
Appendix A. Supplementary data

Fig. S1 FTIR spectra of as-prepared catalysts.

Fig. S2 N_2 adsorption-desorption isotherms of CN and CN@CuCl$_2$.

Fig. S3 Energy band diagrams of CN, CN/CuO/Cu$_2$O-0.10, CN@CuCl$_2$ and CN/CuCl$_2$.

Table S1 XPS analysis results of as-prepared catalysts.

Catalysts	Surface composition				Binding energy (Cu^{1+}/Cu^{2+})	
	C/N	Cu^{1+}/Cu^{2+}	O_{total}/Cu	Cl/Cu	$2p_{3/2}$	$2p_{1/2}$
$CN/CuCl_2$	0.58	1.59	1.83	0.07	932.3/934.6	952.2/955.1
$CN@CuCl_2$	0.72	0.93	0.34	0.12	932.5/934.9	952.4/954.8
$CN/CuO/Cu_2O$-0.10	0.59	1.72	0.39	0.01	932.5/934.1	952.2/954.2
CN	0.49	–	–	–	–	–